High-Dynamic-Range Imaging for Cloud Segmentation

Soumyabrata Dev[1,3], Florian M. Savoy[2], Yee Hui Lee[1], and Stefan Winkler[2]

[1]School of Electrical and Electronic Engineering, Nanyang Technological University (NTU), Singapore 639798
[2]Advanced Digital Sciences Center (ADSC), University of Illinois at Urbana-Champaign, Singapore 138632
[3]The ADAPT SFI Research Centre, Trinity College Dublin, Ireland

Correspondence to: Stefan Winkler (Stefan.Winkler@adsc.com.sg)

Abstract. Sky/cloud images obtained from ground-based sky-cameras are usually captured using a fish-eye lens with a wide field of view. However, the sky exhibits a large dynamic range in terms of luminance, more than a conventional camera can capture. It is thus difficult to capture the details of an entire scene with a regular camera in a single shot. In most cases, the circumsolar region is over-exposed, and the regions near the horizon are under-exposed. This renders cloud segmentation for such images difficult. In this paper, we propose HDRCloudSeg – an effective method for cloud segmentation using High-Dynamic-Range (HDR) imaging based on multi-exposure fusion. We describe the HDR generation process and release a new database to the community for benchmarking. Our proposed approach is the first using HDR images for cloud segmentation and achieves very good results.

1 Introduction

Clouds are one of the important factors in understanding the earth's radiative balance. The analysis of clouds is useful in understanding most of the important weather phenomena. Traditionally, manual observations are performed by *cloud experts* in the WMO (World Meteorological Organization) stations. across the world. Such manual methods are prone to human error, and are expensive. Additionally, weather instruments viz. ceilometers are useful in understanding the vertical profile of the cloud formation. However, they are point-measurement devices, and can provide information in a particular cloud slant path in the atmosphere. Moreover, satellite sensors are also extensively used in monitoring the earth's atmosphere. They are useful to understand climate change, and earth's energy balance (IPCC, 2013; Stephens et al., 2012). However, satellite images have a low temporal- and low spatial- resolution.

Recently, ground-based observations using high-resolution digital cameras are slowly gaining popularity. Whole Sky Imagers (WSIs) are ground-based cameras capturing images of the sky at regular intervals with a wide angle fish-eye lens. They are able to gather high-resolution and localized information about the sky condition at frequent intervals. Due to their low cost and easy setup, their popularity among research groups working in several remote sensing applications is growing. One of the earliest sky cameras were developed by Scripps Institute of Oceanography at the University of California San Diego (Kleissl et al., 2016). It was used to measure sky radiances at various wavelengths. Nowadays, commercial sky cameras are also available. However, such sky imagers are expensive, and have less flexibility in their usage. Therefore, we have designed our sky-camera from off-the-shelf components (Dev et al., 2014b). We use them extensively in our study of cloud analysis in

Singapore. The instantaneous data of cloud formations they provide can be used in weather prediction, solar irradiance modeling (Fua and Cheng, 2013), cloud attenuation prediction (Yuan et al., 2014) and contrail tracking (Schumann et al., 2013). In our research group, we use WSIs to analyze and predict the signal attenuation in satellite-to-ground communication links due to clouds, by monitoring cloud formations along the signal path.

5   While there have been several studies analyzing clouds and their features from WSI images (Long et al., 2006; Souza-Echer et al., 2006; Li et al., 2011; Liu et al., 2015a; Dev et al., 2014a), most of them avoid the circumsolar region, because capturing the details in this area is a non-trivial task. The most popular commercial sky camera is developed by Yankee Environmental Systems, and is referred as *TSI-880* (Long et al., 2001). It is a fully automated sky imager, used in continual monitoring the cloud formation. Its on-board processor computes the cloud coverage and sunshine duration, and stores these results for the

10   user for further processing. However, such imagers capture 8-bit low-dynamic-range image. On a typical sunny and clear day, it is difficult to capture the entire luminance range of the sky scene using a low-dynamic-range image. The region around the sun has a luminous intensity several orders of magnitude higher than other parts of the scene. The ratio between the largest and the smallest luminance value of a scene is referred to as its Dynamic Range (DR).

One of the earliest attempts to capture more of the dynamic range of the sky was done by Stumpfel et al. (2004). They

15   presented a framework in which a set of exposure settings along with neutral density filters are used to generate an HDR composite map. Kenny et al. (2006) used a digital camera to estimate the whole-sky luminance distributions for different sky conditions. Moreover, attempts to provide a full spherical HDR view of the sky/cloud condition were done by mounting hemispherical sky cameras on the top and bottom of airships (Okura et al., 2012). Gryaditskya et al. (2014) used HDR captures of the sky to recover absolute luminance values from images. To the best of our knowledge, there is no prior work that uses

20   the capability of HDR imaging for better segmentation of sky/cloud images. This will greatly assist in the field of solar energy generation and estimation, weather forecasting, and cloud attenuation analysis.

Several techniques for cloud segmentation exist, but they are designed for conventional LDR images. Long et al. (2006) developed a method based on fixed thresholding. As clouds have a non-rigid structure, traditional segmentation algorithms based on shape priors are not applicable. Color is mostly used as a discriminating feature in cloud segmentation (Li et al.,

25   2011; Souza-Echer et al., 2006; Mantelli-Neto et al., 2010). Li et al. (2011) use a hybrid thresholding approach that employs both fixed and adaptive threshold, depending on the bimodality of the input image. Long et al. (2006) model the atmospheric scattering by calculating the ratio of red and blue color channels. Souza-Echer et al. (2006) define appropriate thresholds in the saturation channel of intensity, hue and saturation (IHS) color model. Mantelli-Neto et al. (2010) uses multi-dimensional Euclidean distance to determine the locus of sky and cloud pixels.

30   The motivation of this paper is to propose the use of HDR imaging for cloud segmentation in ground-based sky cameras. We detail the process of image capture and storage in our sky camera system. We show that using HDR images for cloud imaging significantly reduces the amount of saturated pixels in an image, and is therefore an efficient manner to capture the circumsolar region. We define *saturated pixels* for a LDR image as follows: if a particular pixel value is greater than 250 for all of the red-, green- and blue- color channels, then we consider it as saturated. In the case of a tonemapped image, a pixel is considered

35   saturated if that particular pixel is saturated in all its corresponding low-, med- and high- LDR images. Furthermore, HDR

imaging generally provides better segmentation results, as compared to LDR images, regardless of the segmentation method used. In this paper, we show how to improve segmentation results by capturing a larger dynamic range of the sky using High-Dynamic-Range Imaging (HDRI) techniques. We then introduce HDRCloudSeg, a graph-cut based segmentation algorithm that uses the HDR radiance map for accurate segmentation of sky/cloud images.

5   Figure 1 summarizes our proposed approach.

| (a) | (b) | (c) | (d) | (e) |
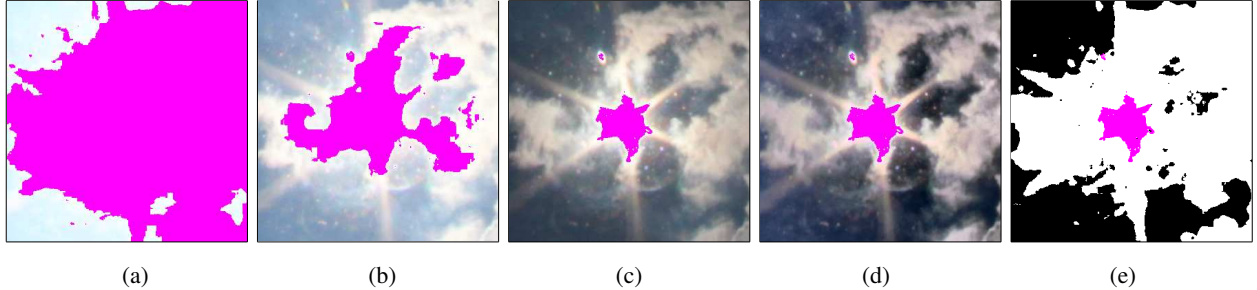
Figure 1. Proposed HDRCloudSeg cloud segmentation approach. (a) High- (b) Mid- (c) Low-exposure Low-Dynamic-Range (LDR) images; (d) Tonemapped High-Dynamic-Range (HDR) image; (e) Binary output using HDRCloudSeg. Saturated pixels in all images are shown in pink. The number of saturated pixels is significantly reduced in the tonemapped HDR image, without compromising on the fine cloud details.

The main novel contributions of the present manuscript include:

– Introducing the use of HDR imaging for better cloud imaging techniques as compared to conventional LDR images. It includes methods and procedures to capture a larger part of the dynamic range of a sky scene and archiving the captured images efficiently;

10   – Proposing a graph-cut based segmentation algorithm that has the best performance as compared to the state-of-the-art algorithms;

– Releasing a database comprising high dynamic captures of the sky scene, along with its manually annotated ground-truth maps[1].

The rest of this paper is structured as follows. We discuss the process of HDRI generation in Section 2. We introduce
15   HDRCloudSeg in Section 3 and evaluate it in Section 4. Section 5 concludes the paper.

2   HDR Image Generation

WAHRSIS, our custom-made sky imagers, are composed of a Digital Single-Lens Reflex (DSLR) camera with a fish-eye lens. They are controlled by a single-board computer housed inside a box with a transparent dome. Our first model (Dev et al., 2014b) used a moving sphere mounted on two motorized arms to block the direct light of the sun. We removed this from our

---

[1] In the final version of this paper, we will release the download link of this database.

latest models in favor of HDR imaging (Dev et al., 2015b). In this way, we avoid potential mechanical problems as well as occlusions in the resulting images.

Typical cameras can only capture a low dynamic range (LDR) image. Therefore, we use the exposure bracketing option of our cameras to capture three pictures at 0, -2 and -4 exposure value (EV) in quick succession. The aperture remains fixed across all captured images, while the shutter speed automatically adapts to match the appropriate exposure. Figure 2 shows an example of the captured images at varying exposure levels. An LDR image taken at low exposure (cf. Fig.2(c)) has few saturated pixels in the circumsolar region, but is underexposed in the regions further from the sun. On the other hand, a high- or mid-exposure LDR image (cf. Fig.2(a) and (b)) can capture the near-horizon regions well, but the circumsolar area becomes over-saturated.

| (a) | (b) | (c) | (d) |
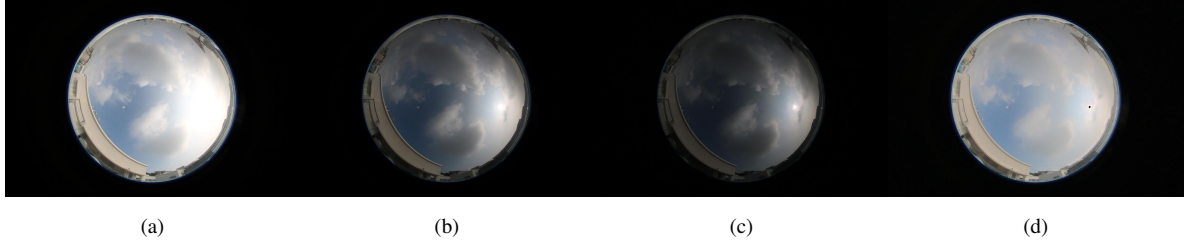
Figure 2. Example of three images captured by the camera at varying exposure levels and shutter speeds. (a) 0 EV, 1/400 sec. (b) -2 EV, 1/1600 sec. (c) -4 EV, 1/4000 sec. (d) Tone-mapped image computed with the pictures (a)–(c).

The different LDR images can then be fused together into a single, high-dynamic-range radiance map. We use Debevec and Malik's algorithm (Debevec and Malik, 1997) to recover HDR radiance map from LDR images. This generated radiance map cannot be viewed directly on a conventional LDR display. Therefore, we tone-map the HDR radiance map into a conventional 8-bit LDR image using contrast-limited adaptive histogram equalization (CLAHE) (Zuiderveld, 1994). We use CLAHE for this application because it involves a logarithmic transformation of the higher DR radiance map to a lower 8-bit display. This produces a perceptually recognizable image, because response of human eye to light is also logarithmic. This operation compresses the dynamic range by preserving the details in the image. Figure 2(d) shows an example of a tone-mapped image.

We also perform the HDR fusion and tone-mapping on a server that collects the images from all our WSIs. Since we have three imagers capturing one frame every 2 minutes, we need algorithms which are computationally efficient. In that context, we use the GPU implementation as referred in Akyüz (2015). It relies on the OpenGL API to perform the entire HDR pipeline on the GPU. It consists of a HDR fusion, which is detailed in the paper itself, followed by tone-mapping, which is based on the photographic tone reproduction operator of Reinhard et al. (2002). Computing a 18 megapixels HDR image and its tone-mapped version takes less than 7 seconds, compared to a few minutes with standard CPU algorithms.

For storage efficiency, we use the *JPEG-XT* format (Richter, 2013) to compress our HDR images[2]. *JPEG-XT* is an extension of *JPEG* currently being developed for HDR images. An important advantage of *JPEG-XT* format is that it is backward

---

[2]We use the reference software source code available at https://jpeg.org/jpegxt/software.html

compatible to the popular *JPEG* compression technique. It consists of a base layer that is compatible with the legacy systems and an extension layer that provides the full dynamic range. Using JPEG-XT at a quality level of 90%, we obtain a file size of about 8 MB. This represents a significant improvement compared to the common *RGBE* format, which uses 50MB per image by storing every pixel with one byte per color channel and one byte as a shared exponent.

3 Cloud Segmentation Using HDRI

We propose a graph-based segmentation algorithm called HDRCloudSeg, that formulates the sky/cloud segmentation task as a graph-partitioning problem. Graph-cut for cloud segmentation was proposed earlier by Liu et al. (2015b). However, Liu et al. used conventional LDR images in their segmentation framework and generated seeds using Otsu threshold (Otsu, 1979). Also, they did not consider the circumsolar regions in their evaluation.

3.1 Notations

Suppose that the low-, mid- and high-exposure LDR sky/cloud images are represented by $\mathbf{X}_i^L$, $\mathbf{X}_i^M$ and $\mathbf{X}_i^H$ respectively, $i = 1, \ldots, N$, where N is the total number of HDR sets in the dataset. Without any loss of generality, $\mathbf{X}_i$ denotes either low-, mid- or high-exposure LDR image in the subsequent sections. Each of these LDR images are *RGB* color images, $\mathbf{X}_i \in \mathbb{R}^{a \times b \times 3}$, having a dimension $a \times b$ for each *R*, *G* and *B* channels. We generate the HDR radiance map $\mathcal{H}_i \in \mathbb{R}^{a \times b \times 3}$ from the set of three LDR images $\mathbf{X}_i^L$, $\mathbf{X}_i^M$ and $\mathbf{X}_i^H$, as described in Section 2.

Let p_{mn} be a sample pixel in the image $\mathbf{X}_i$, where $m = 1, \ldots, a$ and $n = 1, \ldots, b$. We aim to assign labels to each of the pixels p_{mn}, as either *cloud* or *sky*. We denote the label as L_p, where $L_p = 1$ or 0 if p_{mn} is a *cloud* or *sky* pixel, respectively. We model this task as a graph-based discrete labelling problem, wherein we represent $\mathbf{X}_i$ as a graph, comprising a set of nodes and edges.

3.2 Generating Seeds

Graph-cut based segmentation algorithms (Boykov et al., 2001; Kolmogorov and Zabin, 2004; Boykov and Kolmogorov, 2004; Bagon, 2006) require the user to initially label a few pixels as 'foreground' and 'background'. We refer to these prior labeled pixels as *seeds*. The process of generating seeds is generally done manually before partitioning the graph into two sub-graphs. In HDRCloudSeg, we automatically generate these initial seeds by assigning a few pixels in the sky/cloud image with *sky* and *cloud* labels.

Most sky/cloud segmentation algorithms (Li et al., 2011; Long et al., 2006; Souza-Echer et al., 2006; Mantelli-Neto et al., 2010) use color as the discriminating feature to distinguish cloud from sky. In our previous work (Dev et al., 2014a), we have performed a systematic analysis of the existing color spaces and components for conventional LDR images, and observed that color channels, such as $(B - R)/(B + R)$ is one of the most discriminating color channels for cloud segmentation (B and R indicate the blue and red channels of the image). We discuss further details on discriminatory color channels of HDR luminance maps in Section 4.2.1. Furthermore, in Dev et al. (2014a), we have proposed a probabilistic approach for sky/cloud

image segmentation, instead of the conventional binary approach. In this probabilistic approach, each pixel is assigned a *soft* membership to belong to *cloud* category, instead of a *hard* membership.

To illustrate these concepts, consider the example shown in Fig. 3. Figure 3(a) shows a sample LDR sky/cloud image $\mathbf{X}_i$. We extract the $(B-R)/(B+R)$ color channel from this LDR image and show it in Fig. 3(b). A fuzzy c-means clustering on this
5   extracted color channel yields the probabilistic output image, shown in Fig. 3(c). It denotes the confidence level of each pixel to belong to the cloud category. We assume that for a given pixel, the sum of membership values for sky and cloud category is unity.

(a)   (b)   (c)
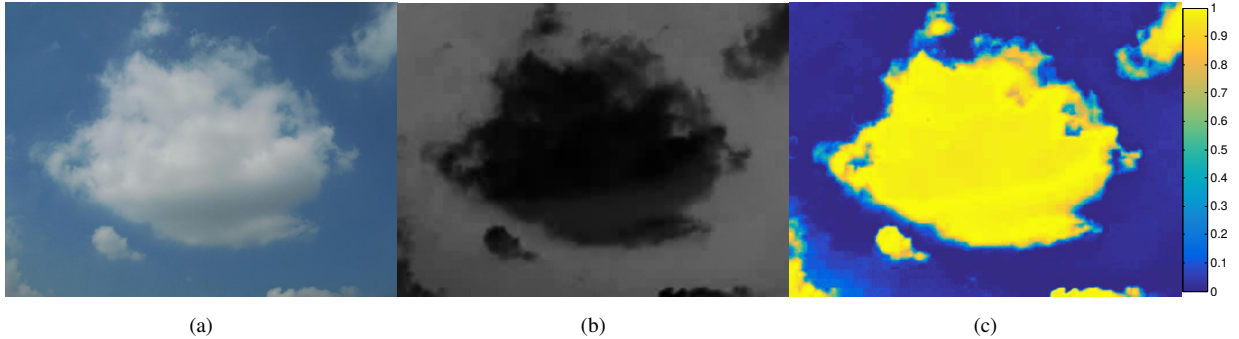
Figure 3. Illustrative example to demonstrate the probability of a pixel belonging to the 'cloud' category. (a) Sample sky/cloud image; (b) $(B-R)/(B+R)$ color channel image; (c) Probabilistic output image using the method from (Dev et al., 2014a).

In HDRCloudSeg, we apply fuzzy c-means clustering to the most discriminatory color channel of the HDR radiance map $\mathcal{H}_i$ to estimate the probability of a pixel belonging to the cloud category. We denote the ratio channel as $\mathbf{Y}_i$. The membership
10   values obtained by clustering provide us a mechanism in assigning the seeds with a degree of confidence. We assign these initial seeds for HDRCloudSeg as follows: pixels having membership $>\alpha$ and $<(1-\alpha)$ are labeled as cloud and sky respectively. The value of α is a constant and is set experimentally (more on this below).

3.3   Partitioning the HDR Graph

The segmentation framework of HDRCloudSeg employs a graph-based image segmentation approach, wherein we represent
15   the ratio-image $\mathbf{Y}_i \in \mathbb{R}^{a \times b}$ as a set of nodes and edges. Each edge of the graph is given a corresponding weight that measures the dissimilarity between two pixels. Such methods are based on *pixel adjacency graphs*, where each vertex is a pixel and the edges between them are defined by adjacency relations. We follow the work of Boykov and Jolly (Boykov and Jolly, 2001) and try to minimize the segmentation score E:

$$E = \sum_{p \in \mathcal{P}} R_p(A_p) + \mu \sum_{(p,q) \in \mathcal{N}; A_p \neq A_q} B_{p,q}, \tag{1}$$

where $R_p(A_p)$ denotes the data cost for an individual pixel p, $B_{p,q}$ denotes the interaction cost between two neighboring pixels p and q in a small neighborhood $\mathcal{N}$, and μ is the weighting parameter.

The complete proposed HDR segmentation algorithm can be summarized as follows:

Algorithm 1 HDRCloudSeg

Require: LDR sky/cloud images with varying EVs.

 1: Create HDR radiance map $\mathcal{H}_i$ from bracketed set of LDR images;

 2: Extract $(B - R)/(B + R)$ ratio channel $\mathbf{Y}_i$ from HDR radiance map $\mathcal{H}_i$;

 3: Perform fuzzy c-means clustering on the extracted ratio channel $\mathbf{Y}_i$ from HDR radiance map $\mathcal{H}_i$, to generate the probabilistic map;

 4: Generate initial seeds from the computed probabilistic map for image segmentation as described in Section 3.2;

 5: Partition the ratio channel $\mathbf{Y}_i$ into two subgraphs using the generated seeds;

 6: **return** Binary segmented image.

We illustrate the complete HDRCloudSeg segmentation framework in Fig. 4. Figure 4(a) represent the three sample LDR images $\mathbf{X}_i^L$, $\mathbf{X}_i^M$ and $\mathbf{X}_i^H$ respectively captured at varying EV settings. We generate the corresponding HDR radiance map $\mathcal{H}_i$ from these LDR images. A tone-mapped version of $\mathcal{H}_i$ is shown in Fig. 4(b), for visualization purposes. We extract the $(B-R)/(B+R)$ ratio channel from $\mathcal{H}_i$, and generate the initial cloud and sky seeds marked in *green* and *red* color respectively, as shown in Fig. 4(c). The binary output image after graph cut is shown in Fig. 4(d).

| (a-i) | (a-ii) | (a-iii) | (b) | (c) | (d) |
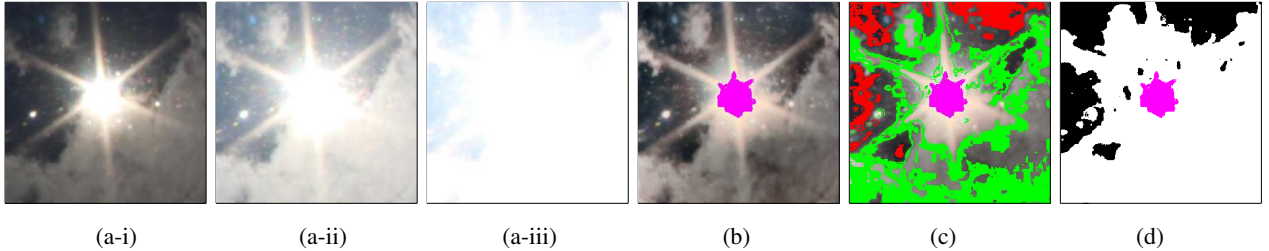
Figure 4. Proposed HDRCloudSeg framework for sky/cloud segmentation. (a) Exposure bracketed Low Dynamic Range (LDR) images; (b) High Dynamic Range (HDR) image tone-mapped for visualization purpose; (c) Image with initial seeds, where *cloud* seeds and *sky* seeds are represented in *green* and *red* respectively; (d) Binary sky/cloud segmentation result. The saturated pixels in (b), (c) and (d) are masked in pink.

4 Experimental Evaluation

4.1 HDR Sky/Cloud Image Database

Currently there are no available HDR image datasets for sky/cloud images. Therefore, in this paper, we propose the first HDR sky/cloud dataset to the research community. We refer this dataset as SHWIMSEG: Singapore HDR Whole Sky Imaging SEGmentation dataset. The SHWIMSEG dataset consists of a total of 156 LDR images, consisting of 52 sets of HDR captures.

Each HDR capture is based on three LDR images (low- ,mid- and high-) which were captured in Automatic Exposure Brack-
eting (AEB) mode of our camera. These high-quality HDR images are captured with our sky imagers, located at the rooftops
of the university building of Nanyang Technological University Singapore. We crop a dimension of 500×500 for all the im-
ages, with the sun location as the geometrical center of the cropped image. The corresponding ground truth images for these
cropped images were manually generated in consultation with experts from the Meteorological Service Singapore (MSS). In
this paper, we release this entire HDR image dataset on sky/cloud image, along with the corresponding raw images for further
benchmarking and extension. Each HDR sets in our dataset comprises the following – original high-resolution captured images
captured in three exposure settings, corresponding 500×500 cropped images with sun in its center, 500×500 ground-truth
maps and the tonemapped images. We perform a detailed evaluation of several cloud segmentation algorithms on this newly
created dataset.

4.2 Results

HDR imaging is an effective technique for cloud observation. It helps us better image the circumsolar region, without satu-
rating the neighboring pixels. We illustrate the advantage of HDR imaging to reduce the saturation by calculating the number
of saturated pixels in the low-, med- and high- LDR images. We also calculate the number of saturated pixels (if any) in
tonemapped images, in the dataset. Using our HDR techniques, we observe that the tonemapped images have 24 times fewer
saturated pixels, as compared to the high-exposure LDR images. Similarly, it has 4 times fewer saturated pixels with respect to
mid- LDR images. A reduced amount of saturated pixels is an important contribution for cloud analysis, especially around the
circumsolar regions.

In addition to containing fewer saturated pixels, HDR imaging also helps in improved cloud segmentation performance,
regardless of the techniques used, as we demonstrate in the following. Cloud segmentation is essentially a binary classification
problem, wherein we classify each pixel as either sky or cloud labels. We report the Precision, Recall and Error values for the
different cloud segmentation methods. Let us suppose that *TP*, *TN*, *FP*, and *FN* denote the true positive, true negative, false
positive and false negative samples in a binary image. Precision, Recall and Error are defined as:

$$\text{Precision} = TP/(TP + FP)$$

$$\text{Recall} = TP/(TP + FN)$$

$$\text{F-score} = \frac{2 \times \text{Precision} \times \text{Recall}}{\text{Precision} + \text{Recall}}$$

$$\text{Error} = (FP + FN)/(TP + TN + FP + FN)$$

For evaluation purposes, we benchmark HDRCloudSeg with existing cloud segmentation algorithms. We consider Li et al.
(2011), Long et al. (2006), Souza-Echer et al. (2006) and Mantelli-Neto et al. (2010). All these existing algorithms, which
were briefly described in Section 1, are designed for conventional LDR images.

4.2.1 Color Channel Selection

In our previous work (Dev et al., 2014a), we have provided a detailed study of various color channels and models, that are conducive for sky/cloud image segmentation. It provides a detailed analysis of the different color channels and components, and also explains why certain ratio color channels are better for cloud segmentation. We use 16 color models and components that are generally used in sky/cloud image segmentation. Table 1 refers the various color channels: it contains the color models $RGB, HSV, YIQ, L^*a^*b^*$, various red and blue ratio channels and chroma channel.

c_1	R	c_4	H	c_7	Y	c_{10}	L^*	c_{13}	R/B	c_{16}	C
c_2	G	c_5	S	c_8	I	c_{11}	a^*	c_{14}	$R-B$		
c_3	B	c_6	V	c_9	Q	c_{12}	b^*	c_{15}	$\frac{B-R}{B+R}$		

Table 1. Color spaces and components used in our analysis. We intend to find the best color channel for HDR imaging.

We designed our proposed HDRCloudSeg segmentation algorithm on the HDR radiance maps. We extract the 16 color channels (as indicated in Table 1) from the HDR radiance map, and perform fuzzy c-means clustering on the extracted color channel. We assign the initial seeds for *cloud* and *sky* pixels in the fuzzy-clustered image; more details on the seeding level in the subsequent Section 4.2.2.
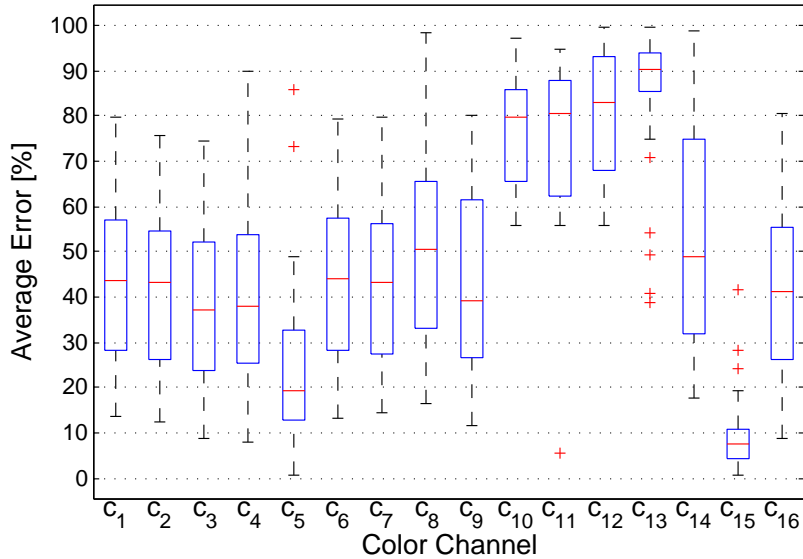
Figure 5. Distribution of the average segmentation error for different color channels, across all the images of the HDR dataset. In each of the individual boxes, the central red mark indicates the median, bottom and top edges indicate the 25th and 75th percentiles respectively.

Figure 5 shows the segmentation error for all the 16 color channels. We observe that the saturation color channel (c_5) and the ratio color channel (c_{15}) has better performance, as compared to other color channels. Therefore, we choose the $(B-R)/(B+R)$ channel as the optimum color channel for HDR segmentation. This color channel is therefore, used in

subsequent experiments. The c_{15} color channel performs the best, owing to a physical phenomenon called Rayleigh scattering. The small particles in the atmosphere scatter light at varying degree. The component of white light having the least wavelength (blue component) gets scattered the most. This renders a bluish color to the sky. The c_{15} color channel is the normalized ratio of *red* and *blue* color channels; and is the most *discriminatory* feature for cloud detection.

4.2.2 Seeding Level Sensitivity

As described in Section 3.2, the value of α determines the amount of initial seeds in HDRCloudSeg. We set a high value of α, because it corresponds to higher confidence in assigning the correct labels. A higher confidence indicates the possibility of low error and high accuracy. We show the Receiver Operating Characteristics (ROC) Curve of our proposed algorithm, for varying values of the seeding parameter. The ROC curve plots the False Positive Rate (FPR) (=$\frac{FP}{FP+TN}$), against the True Positive Rate (TPR) (=$\frac{TP}{TP+FN}$). We generate these points for varying values of α, in the interval $[0, 1]$. This curve helps the user to select the *best* value of the seeding parameter. In order to illustrate its effect on the segmentation performance, we also evaluate the dependency of the seeding parameter on the various evaluation metrics.
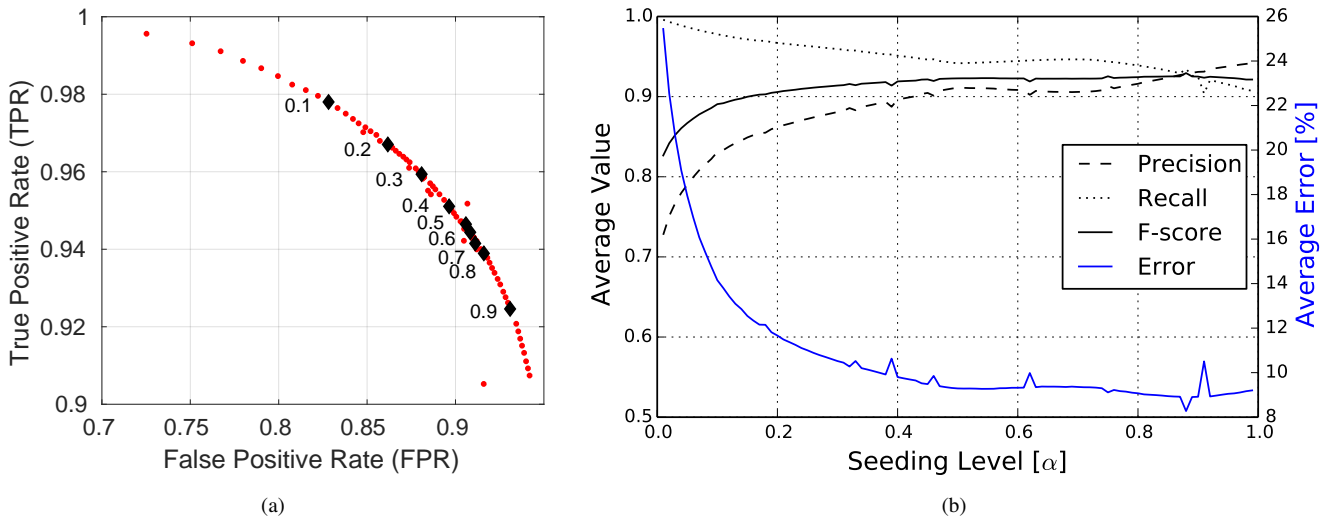
Figure 6. (a) Impact of the seeding parameter on Receiver Operating Characteristics (ROC) Curve; the *diamond* data points indicate the intermediate ROC points, for seeding parameter in intervals of 0.1 in the range $[0,1]$. (b) Impact of the seeding parameter on Average Precision, Recall, F-score value and Average Error. *(Best viewed in color.)*

Figure 6 shows the impact of the seeding value on the average performance of our segmentation framework. We report the average error percentage, precision-, recall- and F-score- value across all the images of the dataset. We observe from Fig. 6 that the average error gradually decreases with increasing value of the seeding parameter, α. This makes sense as higher value of α indicate higher confidence for accurate detection of labels. Similar observations are observed for the average precision, recall and F-score values. The sensitivity of the seeding parameter can also help us in understanding different type of clouds around

the sun aureole. In this manuscript, we deal only with the detection of thick clouds in the circumsolar region. Primarily, this is because, classifying the type of clouds into *thick* or *thin* clouds is an extremely difficult task in the region around the sun. Most of circumsolar region pixels are saturated, owing to its exposure to sun. However, the seeding parameter α has a control on the type of detected clouds. We can detect thin clouds by tuning the seeding parameter, to favor higher cloud detection (i.e. more tendency to classify a pixel as cloud).

From Fig. 6, we observe that there is a dip in the error values when α is set to 0.88. Moreover, at this value, there is a good trade-off between precision and recall values – both precision and recall values are high. Therefore, we experimentally set the value of the seeding parameter, α to 0.88 in the subsequent experiments. We also observe that there are a few deviation points along the curve. The minor *peaks* and *troughs* in Fig. 6 are because of the sensitivity of the considered seeding level. This causes error in the seeding accuracy, that subsequently impacts the final evaluation metric of cloud detection.

4.2.3 Segmentation Performance

Since existing cloud segmentation algorithms are designed for conventional LDR images, we evaluate these current cloud segmentation algorithms on the mid-exposure LDR images as well as the tonemapped images. Our proposed HDRCloudSeg algorithm is the only one designed to make use of the full HDR radiance maps. However, for the sake of comparison, we also evaluate for mid-exposure LDR and tonemapped images. The detailed evaluation results of HDRCloudSeg, along with the other cloud segmentation algorithms, are shown in Table 2.

Methods	Type of image	Precision	Recall	F-score	Error [%]
Long et al.	LDR	0.65	**1.0**	0.77	35.46
	Tonemapped	0.71	0.99	0.82	27.69
Souza et al.	LDR	0.68	0.99	0.79	31.02
	Tonemapped	0.85	0.97	0.89	14.38
Mantelli-Neto et al.	LDR	0.65	**1.0**	0.77	35.22
	Tonemapped	0.68	0.99	0.79	32.11
Li et al.	LDR	0.90	0.85	0.86	16.16
	Tonemapped	0.77	0.99	0.85	21.82
Proposed	LDR	0.86	0.94	0.89	12.83
	Tonemapped	0.83	0.97	0.89	14.96
	HDR	**0.93**	0.93	**0.93**	**8.91**

Table 2. The average scores across all the images are reported for the various benchmark methods. The best performance according to each criterion is indicated in bold.

From Table 2, we observe that HDR imaging improves the cloud segmentation performance, irrespective of the methods used. We observe that most of the benchmark algorithms (except for Li et al.) have a better performance with tonemapped images, as compared to mid-exposure LDR image. This is because a tonemapped version exhibits fewer saturated pixels and clearer contrast between sky and cloud, as compared to the corresponding LDR image. However, our proposed method HDRCloudSeg using the entire HDR luminance map achieves the best error performance of 8.91% across all the methods.

Most of the other algorithms are biased towards a higher recall value (tendency to over-estimate cloud cover), as compared to precision. These existing algorithms are based on a set of thresholds, either fixed or adaptive, and are therefore more prone to high error percentage. However, HDRCloudSeg uses the entire dynamic range of sky/cloud scenes to make a more informed decision in classifying a pixel as cloud or sky.

5   Conclusion & Future work

In this paper, we have proposed a different paradigm to solve cloud segmentation in images captured by WSIs, using High Dynamic Range Imaging (HDRI) techniques. This greatly reduces post-processing steps (image inpainting and de-saturation), unlike sun-blocker based sky camera design. These HDR images capture significantly more details than traditional Low Dynamic Range (LDR) images, especially in the circumsolar region and near the horizon. We have shown that this method outperforms others. Our proposed methodology is reliable, efficient and easy to be deployed across any weather conditions. Moreover, because of the recent advances in the photogrammetric techniques, it is easy to implement HDR-based segmentation algorithms in sky cameras.

In our future work, we plan to investigate how High Dynamic Range imaging improves the accuracy of other tasks, such as cloud classification (Dev et al., 2015a) or cloud height estimation (Savoy et al., 2015). In order to improve benchmarking, we will also work on expanding the sky/cloud HDR dataset introduced here. We will extend the dataset to a ternary ground-truth map dataset, consisting of *clear sky*, *thin clouds*, and *thick clouds*.

6   Code availability

The source code of all simulations in this paper is available online at `https://github.com/Soumyabrata/HDR-cloud-segmentation`. These codes are released with the spirit of reproducible research (Vandewalle et al., 2009).

7   Data availability

The download link of the entire HDR sky/cloud image dataset, along with the corresponding ground-truth maps will be available in the final version. This will help the community for further benchmarking analysis.

Acknowledgements. This research is funded by the Defence Science and Technology Agency (DSTA), Singapore.

References

Akyüz, A. O.: High dynamic range imaging pipeline on the GPU, Journal of Real-Time Image Processing, 10, 273–287, 2015.

Bagon, S.: Matlab wrapper for graph cut, 2006.

Boykov, Y. and Jolly, M.-P.: Interactive graph cuts for optimal boundary & region segmentation of objects in N-D images, in: Proc. Interna-
5   tional Conference on Computer Vision (ICCV), 2001.

Boykov, Y. and Kolmogorov, V.: An experimental comparison of min-cut/max-flow algorithms for energy minimization in vision, IEEE
transactions on pattern analysis and machine intelligence, 26, 1124–1137, 2004.

Boykov, Y., Veksler, O., and Zabih, R.: Fast approximate energy minimization via graph cuts, IEEE Transactions on pattern analysis and
machine intelligence, 23, 1222–1239, 2001.

10 Debevec, P. E. and Malik, J.: Recovering High Dynamic Range Radiance Maps from Photographs, in: Proc. 24th Annual Conference on
Computer Graphics and Interactive Techniques, 1997.

Dev, S., Lee, Y. H., and Winkler, S.: Systematic Study of Color Spaces and Components for the Segmentation of Sky/Cloud Images, in: Proc.
International Conference on Image Processing (ICIP), pp. 5102–5106, 2014a.

Dev, S., Savoy, F. M., Lee, Y. H., and Winkler, S.: WAHRSIS: A low-cost, high-resolution whole sky imager with near-infrared capabilities,
15   in: Proc. IS&T/SPIE Infrared Imaging Systems, 2014b.

Dev, S., Lee, Y. H., and Winkler, S.: Categorization of cloud image patches using an improved texton-based approach, in: Proc. International
Conference on Image Processing (ICIP), pp. 422–426, 2015a.

Dev, S., Savoy, F. M., Lee, Y. H., and Winkler, S.: Design of low-cost, compact and weather-proof whole sky imagers for High-Dynamic-
Range captures, in: Proc. International Geoscience and Remote Sensing Symposium (IGARSS), pp. 5359–5362, 2015b.

20 Fua, C.-L. and Cheng, H.-Y.: Predicting solar irradiance with all-sky image features via regression, Solar Energy, 97, 537–550, 2013.

Gryaditskya, Y., Pouli, T., Reinhard, E., and Seidel, H.-P.: Sky Based Light Metering for High Dynamic Range Images, Computer Graphics
Forum, 33, 61–69, 2014.

IPCC: Climate Change 2013: The Physical Science Basis, Tech. rep., Intergovernmental Panel on Climate Change (IPCC), 2013.

Kenny, P., Olley, J. A., and Lewis, J. O.: Whole-Sky Luminance Maps from Calibrated Digital Photography, in: Proc. EuroSun Conference,
25   2006.

Kleissl, J., Urquhart, B., Ghonima, M., Dahlin, E., Nguyen, A., Kurtz, B., Chow, C. W., and Mejia, F. A.: University of California, San Diego
(UCSD) Sky Imager Cloud Position Study Field Campaign Report, Tech. rep., DOE ARM Climate Research Facility, Washington, DC
(United States), 2016.

Kolmogorov, V. and Zabin, R.: What energy functions can be minimized via graph cuts?, IEEE transactions on pattern analysis and machine
30   intelligence, 26, 147–159, 2004.

Li, Q., Lu, W., and Yang, J.: A Hybrid Thresholding Algorithm for Cloud Detection on Ground-Based Color Images, Journal of Atmospheric
and Oceanic Technology, 28, 1286–1296, 2011.

Liu, S., Zhang, L., Zhang, Z., Wang, C., and Xiao, B.: Automatic Cloud Detection for All-Sky Images Using Superpixel Segmentation, IEEE
Geoscience and Remote Sensing Letters, 12, 354–358, 2015a.

35 Liu, S., Zhang, Z., Xiao, B., and Cao, X.: Ground-Based Cloud Detection Using Automatic Graph Cut, IEEE Geoscience and Remote
Sensing Letters, 12, 1342–1346, 2015b.

Long, C. N., Slater, D. W., and Tooman, T.: Total sky imager model 880 status and testing results, Tech. rep., DOE Office of Science Atmospheric Radiation Measurement (ARM) Program (United States), 2001.

Long, C. N., Sabburg, J. M., Calbó, J., and Pages, D.: Retrieving Cloud Characteristics from Ground-Based Daytime Color All-Sky Images, Journal of Atmospheric and Oceanic Technology, 23, 633–652, 2006.

5 Mantelli-Neto, S. L., von Wangenheim, A., Pereira, E. B., and Comunello, E.: The Use of Euclidean Geometric Distance on RGB Color Space for the Classification of Sky and Cloud Patterns, Journal of Atmospheric and Oceanic Technology, 27, 1504–1517, 2010.

Okura, F., Kanbara, M., and Yokoya, N.: Full Spherical High Dynamic Range Imaging from the Sky, in: Proc. International Conference on Multimedia & Expo (ICME), 2012.

Otsu, N.: A Threshold Selection Method from Gray-Level Histograms, IEEE Transactions on Systems, Man, and Cybernetics, 9, 62–66, 10 1979.

Reinhard, E., Stark, M., Shirley, P., and Ferwerda, J.: Photographic tone reproduction for digital images, ACM transactions on graphics (TOG), 21, 267–276, 2002.

Richter, T.: On the standardization of the JPEG XT image compression, in: Proc. Picture Coding Symposium (PCS), pp. 37–40, 2013.

Savoy, F. M., Lemaitre, J., Dev, S., Lee, Y. H., and Winkler, S.: Cloud base height estimation using high-resolution whole sky imagers, in: 15 Proc. International Geoscience and Remote Sensing Symposium (IGARSS), pp. 1622–1625, 2015.

Schumann, U., Hempel, R., Flentje, H., Garhammer, M., Graf, K., Kox, S., Losslein, H., and Mayer, B.: Contrail study with ground-based cameras, Atmospheric Measurement Techniques, 6, 3597–3612, 2013.

Souza-Echer, M. P., Pereira, E. B., Bins, L. S., and Andrade, M. A. R.: A simple method for the assessment of the cloud cover state in high-latitude regions by a ground-based digital camera, Journal of Atmospheric and Oceanic Technology, 23, 437–447, 2006.

20 Stephens, G. L., Li, J., Wild, M., Clayson, C. A., Loeb, N., Kato, S., Lecuyer, T., Jr, P. W. S., Lebsock, M., and Andrews, T.: An update on Earth's energy balance in light of the latest global observations, Nature Geoscience, 5, 691, 2012.

Stumpfel, J., Tchou, C., Jones, A., Hawkins, T., Wenger, A., and Debevec, P.: Direct HDR Capture of the Sun and Sky, in: Proc. 3rd International Conference on Computer Graphics, Virtual Reality, Visualisation and Interaction in Africa, 2004.

Vandewalle, P., Kovacevic, J., and Vetterli, M.: Reproducible research in signal processing, IEEE Signal Processing Magazine, 26, 2009.

25 Yuan, F., Lee, Y. H., and Meng, Y. S.: Comparison of radio-sounding profiles for cloud attenuation analysis in the tropical region, in: Proc. IEEE International Symposium on Antennas and Propagation, pp. 259–260, 2014.

Zuiderveld, K.: Graphics Gems IV, pp. 474–485, Academic Press Professional, Inc., 1994.